




Article

Spin Gapless Semiconductor–Nonmagnetic Semiconductor Transitions in Fe-Doped Ti_2CoSi : First-Principle Calculations

Yu Feng ¹, Zhou Cui ¹, Ming-sheng Wei ¹, Bo Wu ^{2,3,*} and Sikander Azam ⁴

¹ School of Physics and Electronic Engineering, Jiangsu Normal University, Xuzhou 221116, China; fengyu@jsnu.edu.cn (Y.F.); zhoucuijsnu@163.com (Z.C.); weims@jsnu.edu.cn (M.-s.W.)

² School of Physics and Electronic Science, Zunyi Normal University, Zunyi 563002, China

³ School of Marine Science and Technology, Northwestern Polytechnical University, Xi'an 710072, China

⁴ Department of Physics, The University of Lahore, Sargodha Campus, Sargodha 40100, Pakistan; sikander.physicst@gmail.com

* Correspondence: fqwubo@zync.edu.cn; Tel.: +86-0851-2892-7153

Received: 28 October 2018; Accepted: 6 November 2018; Published: 9 November 2018



Abstract: Employing first-principle calculations, we investigated the influence of the impurity, Fe atom, on magnetism and electronic structures of Heusler compound Ti_2CoSi , which is a spin gapless semiconductor (SGS). When the impurity, Fe atom, intervened, Ti_2CoSi lost its SGS property. As Ti^{A} atoms (which locate at (0, 0, 0) site) are completely occupied by Fe, the compound converts to half-metallic ferromagnet (HMF) TiFeCoSi . During this SGS→HMF transition, the total magnetic moment linearly decreases as Fe concentration increases, following the Slater–Pauling rule well. When all Co atoms are substituted by Fe, the compound converts to nonmagnetic semiconductor Fe_2TiSi . During this HMF→nonmagnetic semiconductor transition, when Fe concentration y ranges from $y = 0.125$ to $y = 0.625$, the magnetic moment of Fe atom is positive and linearly decreases, while those of impurity Fe and Ti^{B} (which locate at (0.25, 0.25, 0.25) site) are negative and linearly increase. When the impurity Fe concentration reaches up to $y = 1$, the magnetic moments of Ti, Fe, and Si return to zero, and the compound is a nonmagnetic semiconductor.

Keywords: Heusler alloy; electronic structure; magnetism; doping

1. Introduction

As one of the most outstanding material classes, Heusler compounds with a chemical formula of X_2YZ are a large family containing more than 1500 members [1,2]. When the number of valence electrons (VEs) of X atom is more than that of Y atom, Heusler compounds are known to be of a conventional type, i.e., Cu_2MnAl type with a space group of FM-3M, see Figure 1a [3]. While, when the number of VEs of X atom is less than that of Y atom, Heusler compounds crystallize in an inverse type, i.e., Hg_2CuTi type with space group of F-43M, see Figure 1b [4]. In addition, when two X atoms are different, the chemical formula of Heusler compounds converts to $\text{XX}'\text{YZ}$, and it is a quaternary type, i.e., LiMgPbSn type with space group of F-43M, see Figure 1c [5,6]. Owing to the fact that there is huge number of Heusler compounds that could be comprised by a combination of different elements, Heusler compounds exhibit diverse properties. Several Heusler compounds, such as Co_2MnSi , Ti_2CoAl , CoFeMnAl , and others, have been theoretically predicted and experimentally confirmed to be half-metallic ferromagnets [7–13]. Due to the special band structure, that the majority of the band shows metallicity, while an energy gap exists in the minority band, half-metallic Heusler compounds could offer theoretically 100% spin-polarized current. Besides, most of the half-metallic Heusler compounds possess high Curie temperature, and their lattice constants are very close to many

semiconductors, such as MgO and GaAs. They are, therefore, regarded as one of the most excellent candidates for electrode materials of spintronics devices, such as magnetic tunnel junctions (MTJ) and current-perpendicular-to-plane spin valves (CPP-SV), and have a great application potential in magnetic random access memory (MRAM), ultra-high-speed reading in magnetic read heads of hard disk drivers (HDD) and spin transfer torque (STT) devices in spin random access memory [14–21]. In addition, a lot of Heusler compounds, especially half-Heusler compounds with chemical formula of XYZ, exhibit semiconductor character. Owing to high Seebeck coefficient, large electrical conductivity, good thermal stability, and environmentally friendly constituents, semiconducting Heusler compounds, such as *n*-type MNiSn (M = Ti, Zr, Hf) and *p*-type ErNiSn, HfPtSn, became promising thermoelectric materials which could recycle waste heat into electricity [22–25]. Hence, they are great useful for wearable devices like smart watches, and for sensors in industrial process monitoring. More recently, much attention has been paid to a new subfamily of Heusler compounds which were characterized with a novel band structure, that there is an energy gap that lies in minority bands, while the valence and conduction band edges of the majority of electrons touch at Fermi level, resulting in a zero-width gap. They are, therefore, classified to be spin gapless semiconductors (SGSs) [26]. Heusler compound Mn₂CoAl with SGS properties has been successfully fabricated, and high Curie temperature (T_C) of 720 K as well as magnetism of 2 μ_B were detected [27–29]. Others, like Ti₂CoSi and CoFeCrGa, also received intense research interest [30–34]. Owing to the extraordinary band structure, both electrons and holes of SGS Heusler compounds can be spin-polarized, and almost no threshold energy is required to move electrons from the valence band to the conduction band, as the mobility of carriers is stronger than that in regular semiconductors. Hence, they are considered to be possible candidates to substitute for diluted magnetic semiconductors (DMS) [35]. Due to the reason that diverse valence electrons configurations of Heusler compounds result in varied magnetic properties and electronic structures, in this paper, we studied the influence of impurity Fe atom on magnetism and electronic structures of Heusler compound Ti₂CoSi.

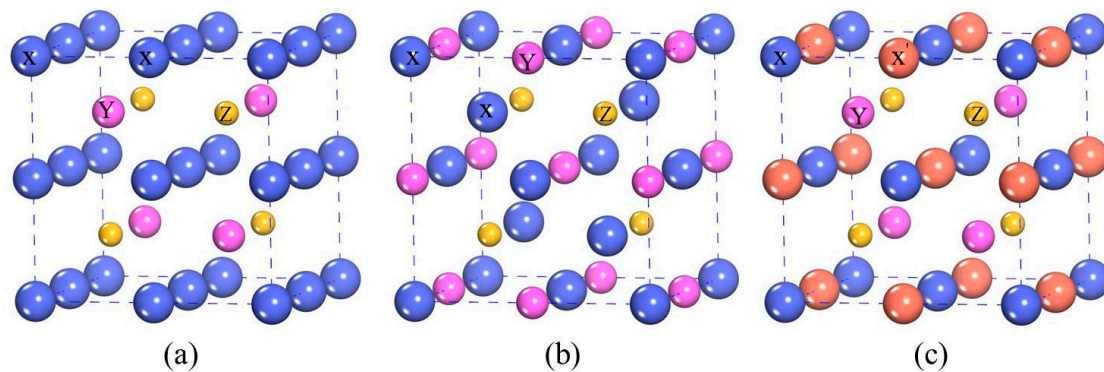


Figure 1. Schematic representation of (a) Cu₂MnAl-type Heusler compound; (b) Hg₂CuTi-type Heusler compound; (c) LiMnPbSn-type Heusler compound.

2. Structures and Calculation Methods

All calculations are performed by employing the VASP Package based on the density functional theory (DFT) [36]. Plane-wave basis sets, together with the projector-augmental wave (PAW) [37] method, are chosen to deal with electron–ion interaction. The valence-electron configurations of Ti ($3d^24s^2$), Fe ($3d^64s^2$), Co ($3d^74s^2$), and Si ($3s^23p^2$) are selected. The $7 \times 7 \times 7$ mesh of special k-points in the Brillouin zone is applied. In the self-consistent calculation, we select the refined 1×10^{-6} eV/atom as the SCF convergence criterion, and 360 eV as energy cutoff, respectively. When the positions of atoms are relaxed, we set a convergence criterion of 0.02 eV/Å. All structures are built with $2 \times 1 \times 1$ supercell. For the doped compound calculations, we geometrically optimize all supercells by using the same parameters employed in the bulk calculation. All technical parameters have been tested carefully to ensure the accuracy of the results.

3. Results and Discussion

Interface Structures

The electronic structure of Ti_2CoSi is firstly calculated. In Figure 2, there is a large energy gap of 0.671 eV exists in spin down band, and the Fermi level locates at the top of the gap. Such an energy gap is a result of exchange splitting between spin down unoccupied antibonding bands (which are localized at Co, Ti^{A} and Ti^{B} atoms) and spin down occupied bands (which are predominantly of Co character). As for spin up band, it exhibits an obvious zero-width gap around the Fermi level. It also can be seen from Figure 3 that the maximum of the valence band sits at Γ point, while the minimum of the conduction bands locates at X point; such a closed spin up gap, therefore, is an indirect gap.

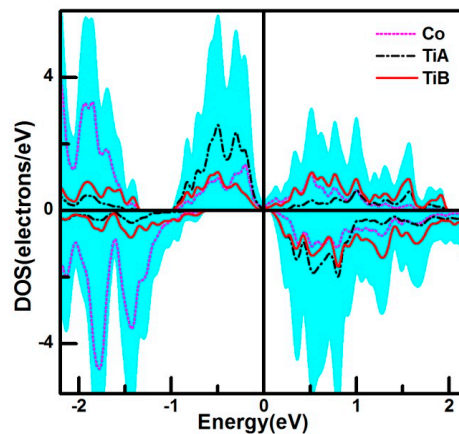


Figure 2. The electronic structure of Ti_2CoSi .

When Fe atom is introduced into Ti_2CoSi , it could lead to four doping structures, thus, X(Fe) doping structure where X atom ($X = \text{Ti}^{\text{A}}, \text{Ti}^{\text{B}}, \text{Co}, \text{Si}$) is substituted by an Fe atom. In order to determine which doping structure is more favorable, the formation energy is calculated by the following equation $E_f = E' - E - \sum_i n_i \mu_i$, where E_f is formation energy, and E' and E are total energy of the doping structure and undoping structure, respectively. The integer n_i is the number of atoms that has been removed from (n_i is negative value) or added to (n_i is positive value) to form the disorders, and μ_i is the corresponding chemical potential which represents the energy of the reservoirs. According to our calculation, the highest E_f of 1.028 eV belongs to $\text{Ti}^{\text{B}}(\text{Fe})$ doping structure, and that of $\text{Co}(\text{Fe})$ and $\text{Si}(\text{Fe})$ are also as high as -0.023 eV and -0.018 eV, respectively, while the minimal E_f of -0.927 eV occurs in $\text{Ti}^{\text{A}}(\text{Fe})$ doping structure. It reveals that $\text{Ti}^{\text{B}}, \text{Co}$, and Si atoms are hard to be replaced by Fe atom, however, Ti^{A} atom could be easily replaced with Fe atom. Therefore, we focus on the $\text{Ti}^{\text{A}}_{1-x}\text{Fe}_x\text{Ti}^{\text{B}}\text{CoSi}$ doping structure, where the doping concentration $x = 0, 0.125, 0.25, 0.375, 0.5, 0.625, 0.75, 0.875$, and 1.

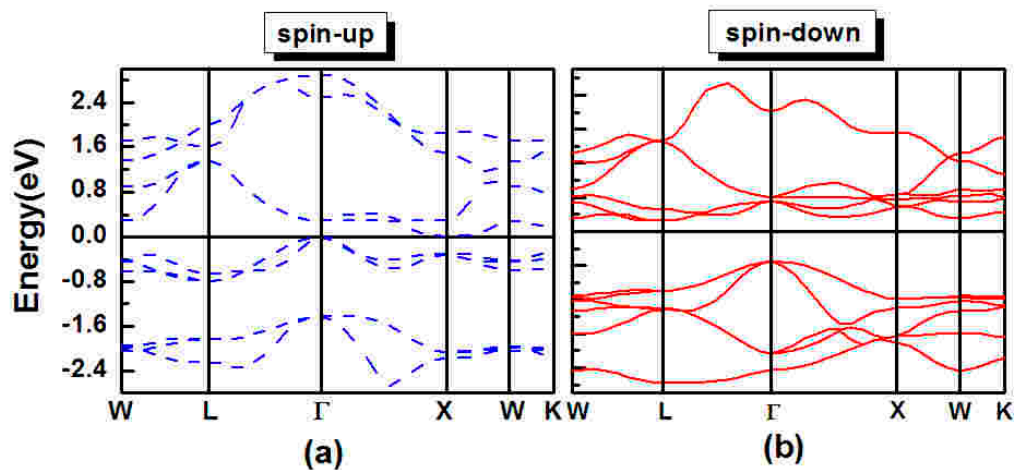


Figure 3. The band structure of Ti_2CoSi . (a) Spin-up band structure. (b) Spin-down band structure.

In Figure 4, when the Fe atom intervenes in Ti_2CoSi and the doping concentration increases, the zero-width gap in spin up states is destroyed, and the spin up band strides over the Fermi level and shows metallic behavior. On the other hand, doping Fe atom produces a negative impact on the spin down energy gap, causing the width of the gap to vanish, and the Fermi level drops into a spin down conduction band. As a result, the SGS character of Ti_2CoSi is completely destroyed by the impurity Fe atom. When the doping concentration $x = 0.875$, the top of the spin down valence band and the bottom of spin down conduction band touch at Fermi level, and form an indirect closed spin down gap. The doping structure, $\text{Ti}^{\text{A}}_{0.125}\text{Fe}_{0.875}\text{Ti}^{\text{B}}\text{CoSi}$, is a gapless half-metal. As the doping concentration increases up to $x = 1$, the closed spin down gap is opened, while the spin up states still cross the Fermi level. Therefore, when $x = 1$, the structure converts to a quaternary Heusler alloy TiFeCoSi with half-metallic character.

It can be seen from Figure 5 that TiFeCoSi possesses a wide half-metallic energy gap of about 0.56 eV, and the Fermi level is located slightly above the middle of the gap and, hence, it is predicted to have stable half-metallicity. Both spin down occupied bonding bands and spin down unoccupied antibonding bands are mainly localized by Co and Fe atoms. Figure 6 shows the half-metallicity of TiFeCoSi as a function of the lattice constant, and it holds the half-metallic energy gap when its lattice constant increases from 5.4 Å to 6.1 Å. When the lattice constant is 5.4 Å, the Fermi level lies at the top of spin down valence band, and when TiFeCoSi is further compressed, the Fermi level would drop into the valence band and lose its half-metallicity. With the lattice constant increases, the Fermi level gradually moves from a low energy zone to a high energy zone. As the lattice constant increases up to 6.1 Å, the Fermi level locates at the bottom of spin down conduction band, and when TiFeCoSi is further stretched, the Fermi level would move into the conduction band, and half-metallicity is also destroyed.

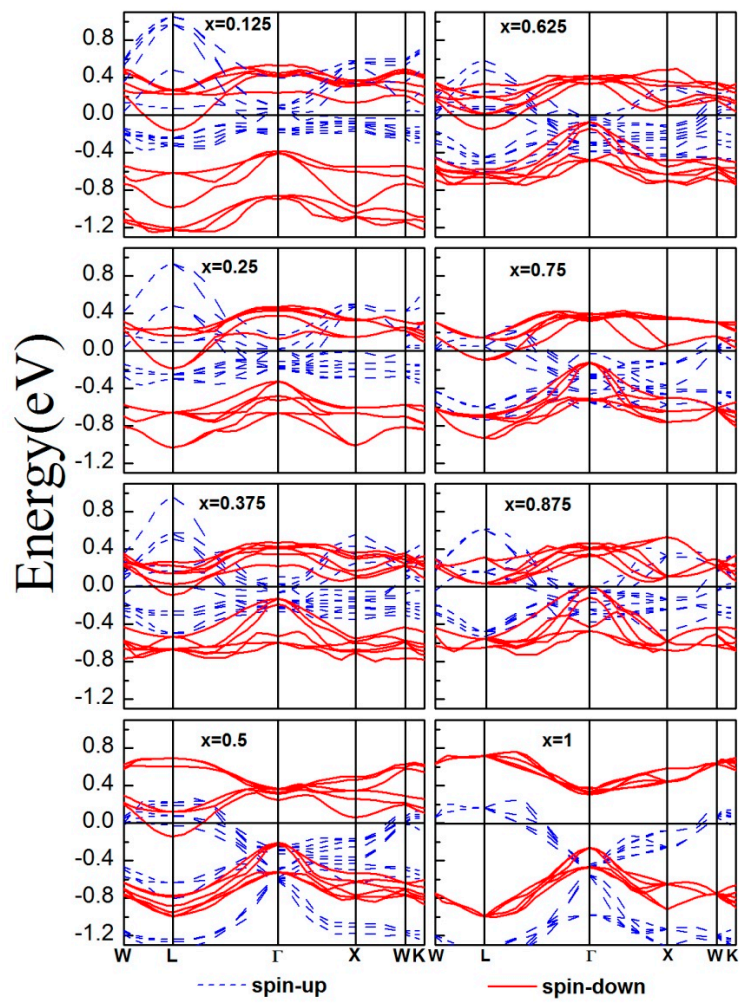


Figure 4. The band structures of $Ti^A_{1-x}Fe_xTi^B CoSi$.

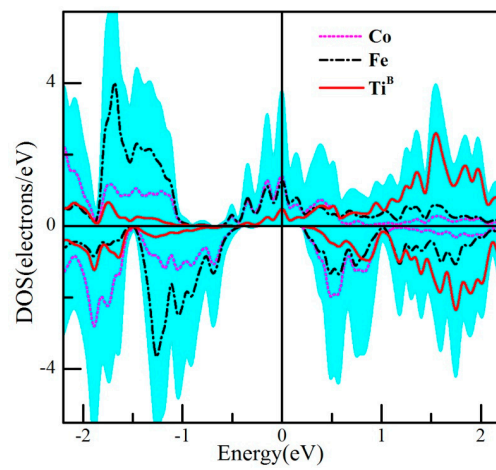


Figure 5. The electronic structure of $TiFeCoSi$.

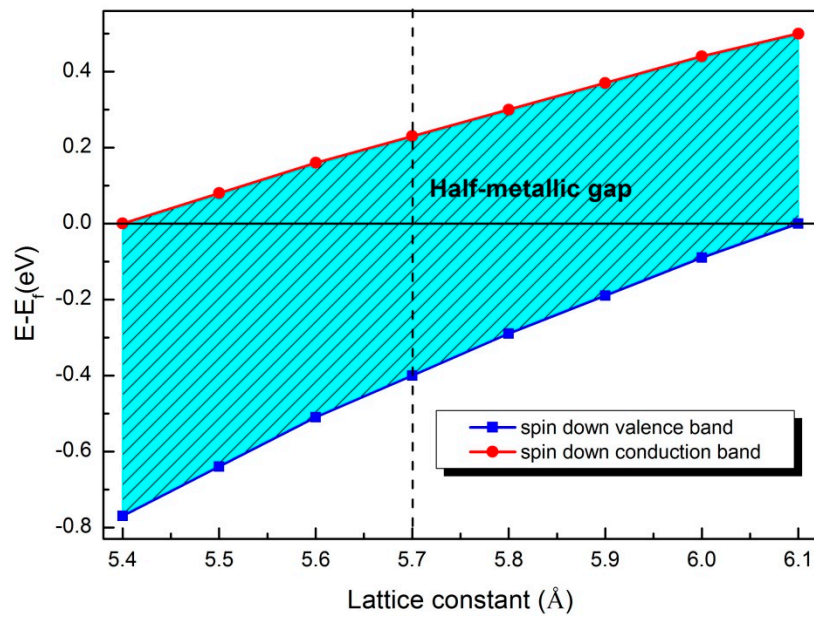


Figure 6. Dependence of the half-metallic state on the lattice constant. The dotted line indicates the half-metallic state at equilibrium lattice constant.

The atom-resolved spin magnetic moment (AMM) and total magnetic moment (TMM) of Fe doped Ti_2CoSi as a function of Fe concentration is shown in Figure 7. As for pure Ti_2CoSi , Ti^{A} and Ti^{B} contribute the main part of TMM, while Co offers a small part, due to the reason that low valence transition metal Ti atom has larger spin splitting than the high valence transition metal Co. When Fe atom doping in Ti_2CoSi forms $\text{Ti}^{\text{A}}_{1-x}\text{Fe}_x\text{Ti}^{\text{B}}\text{CoSi}$, the contribution of Fe atom to the TMM is lower than Ti^{A} atom. As the Fe doping concentration increases, the AMM of Ti^{A} , Ti^{B} , and Fe atoms lineally decline, while AMM of the Co atom is enhanced, and it is almost as high as Fe atom when the doping concentration increases to $x = 1$. It also can be seen that when x ranges from 0 to 0.625, the AMMs of Ti^{A} , Ti^{B} , Fe, and Co are positive values, indicating the ferromagnetic arrangement among these transition metal elements. While, when $x > 0.625$, the AMM of Ti^{B} atom reverses to a negative value, leading to the fact that the doped structure changes into a ferrimagnet. Overall, the TMM lineally decreases with Fe concentration increases, and it is in good agreement with the Slater–Pauling rule, which can be written as $\text{TMM} = Z - 24$, where Z is the total number of valence electrons.

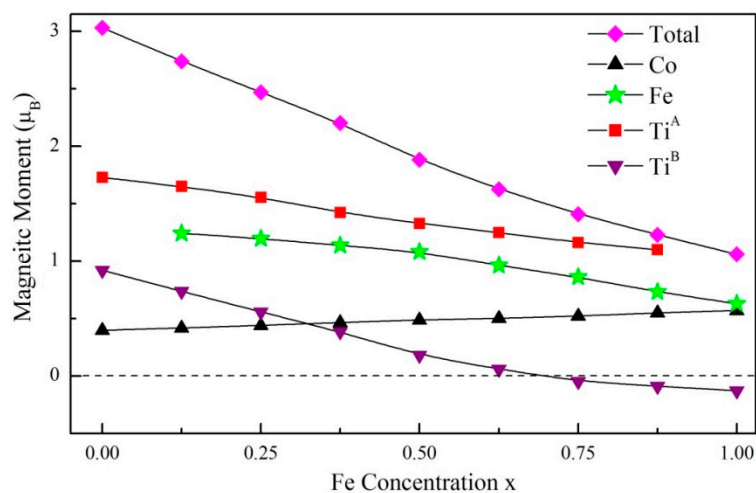


Figure 7. The calculated total magnetic moment and atom-resolved spin magnetic moments (AMMs) of the Co, Fe, Ti^{A} , and Ti^{B} atoms of $\text{Ti}^{\text{A}}_{1-x}\text{Fe}_x\text{Ti}^{\text{B}}\text{CoSi}$ as a function of impurity Fe concentration x .

Based on the half-metallic TiFeCoSi, we continue to introduce the impurity, Fe atom, and impurity Fe may occupy Ti, Co, or Si atoms, forming a Ti(Fe), Co(Fe), or Si(Fe) doping structure, respectively. The formation energy of these three possible doping structures are also calculated by Equation (1). Si(Fe) and Ti(Fe) doping structures respectively exhibit high formation energies of 1.895 eV and 1.437 eV, revealing that Si and Ti are hard to be replaced by Fe atom. While Co(Fe) doping structure possesses the minimal formation energy of -0.153 eV, indicating that the Co atom is easily occupied by Fe atom and forms the $\text{TiFeCo}_{1-y}\text{Fe}_y\text{Si}$ doping structure, where y is the concentration of the impurity Fe atom, and $y = 0.125, 0.25, \dots, 0.875, 1$. Figure 8 shows the band structures of $\text{TiFeCo}_{1-y}\text{Fe}_y\text{Si}$. When impurity Fe concentration y ranges from 0.125 to 0.625, spin up bands stride over the Fermi level, while there is an obvious energy gap that exists in the spin down bands. Therefore, $\text{TiFeCo}_{1-y}\text{Fe}_y\text{Si}$ maintains its half-metallicity when the impurity Fe concentration increases from 0.125 to 0.625. As y increases to 0.75, the Fermi level drops into the spin down conduction band, and the doping structure loses its half-metallicity, and the spin polarization decreases to about 74%. In addition, with an increase of the impurity Fe concentration, the overlap degree between spin up valence band and spin down valence band increases. When y reaches up to 0.875, the Fermi level still exists in the spin down conduction band, and there is much overlap between the spin up and spin down bands, and the energies of the spin up and spin down bands are almost the same, making the spin polarization seriously drop to only 3%. Hence, the doping structure $\text{TiFeCo}_{0.125}\text{Fe}_{0.875}\text{Si}$ can be regarded as pseudo-semiconductor. As the impurity Fe concentration further increases up to $y = 1$, the spin up and spin down bands completely overlap, and there is an energy gap of 0.418 eV that exists in both spin up and spin down band, and the structure Fe_2TiSi therefore converts to a semiconductor.

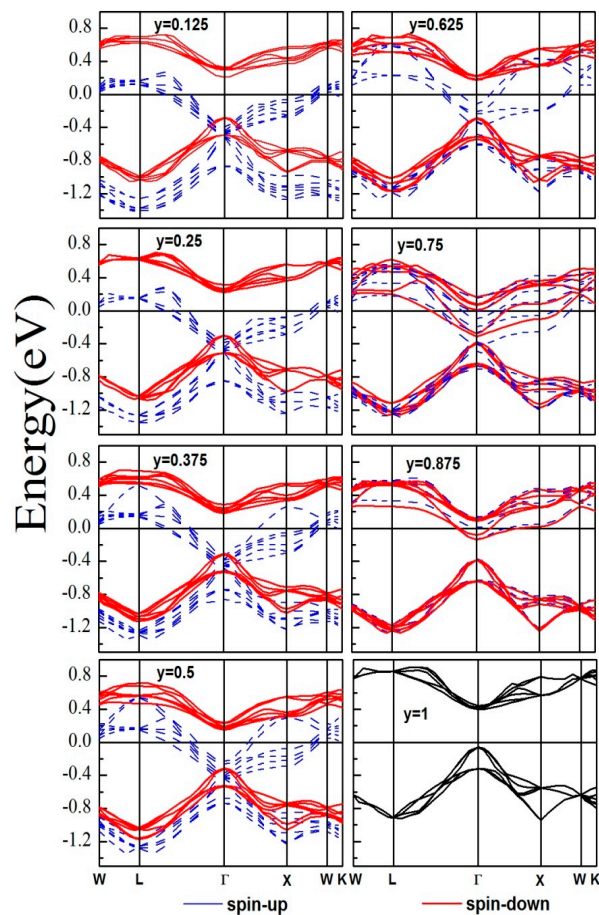


Figure 8. The band structures of $\text{TiFeCo}_{1-y}\text{Fe}_y\text{Si}$.

The AMM and TMM of Fe doped TiFeCoSi as a function of impurity Fe concentration is exhibited in Figure 9. When impurity Fe concentration increases from 0.125 to 0.75, AMM of Co atom has a slight increase, while that of the Fe atom descends obviously. In addition, the absolute value of AMMs of Ti^B and impurity Fe are weakened. It should be noted that when the impurity Fe concentration y increases to 0.875, the AMM of Co atom suffers a sharp decline, and AMMs of all atoms are extremely close to zero, owing to the fact that $TiFeCo_{0.125}Fe_{0.875}Si$ shows a pseudo-semiconductor property. Furthermore, AMMs of Co and Fe are positive values, while that of Ti^B and impurity Fe are negative values, indicating that doping structure $TiFeCo_{1-y}Fe_ySi$ is a ferrimagnet when y ranges from 0.125 to 0.75. As the impurity Fe concentration further increases up to $y = 1$, AMMs of all atoms are zero. As a result, Fe_2TiSi is a nonmagnetic semiconductor.

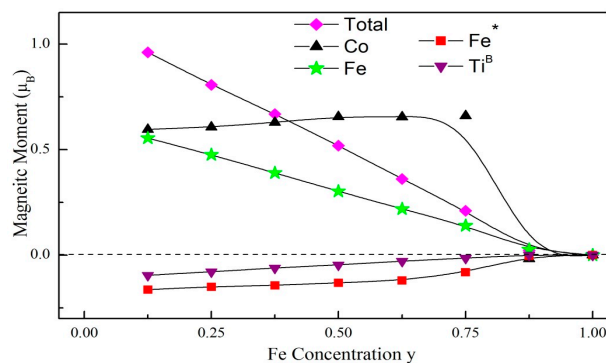


Figure 9. The calculated total magnetic moment and atom-resolved spin magnetic moments (AMMs) of the Co, Fe, Ti^B , and impurity Fe (Fe^*) atoms of the $TiFeCo_{1-y}Fe_ySi$ as a function of impurity Fe concentration y .

4. Conclusions

We investigated the influence of impurity Fe atom on magnetism and electronic structures of Heusler compound Ti_2CoSi by using the first-principle calculations within density functional theory (DFT). Ti_2CoSi is a spin gapless semiconductor (SGS) with an indirect closed spin down energy gap. It lost its SGS property when the impurity Fe atom intervened, and when the concentration of impurity Fe atom increases to $x = 0.875$, the compound shows gapless metal character. At the doping concentration of $x = 1$, Ti^A atoms are completely occupied by impurity Fe atoms, and the compound converts to $TiFeCoSi$, which is a half-metallic ferromagnet (HMF). During this SGS→HMF transition, the total magnetic moment linearly decreases with the concentration of impurity Fe atom increasing, which follows the Slater–Pauling rule well. When the impurity Fe further increases from $y = 0.125$ to $y = 0.625$, the doping compounds maintain their half-metallicity. While, when the doping concentration increases up to $y = 1$, the compound converts to semiconductor Fe_2TiSi . During this HMF→nonmagnetic semiconductor transition, when the concentration of impurity Fe atom ranges from $y = 0.125$ to $y = 0.625$, the magnetic moment of Fe atom is positive and linearly decreases, while that of impurity Fe and Ti^B are negative and linearly increase. When all Co atoms are substituted by Fe atoms, the magnetic moments of Ti, Fe, and Si return to zero, and the compound, therefore, is a nonmagnetic semiconductor.

Author Contributions: Methodology, Z.C.; software, M.-s.W. and S.A.; writing—original draft preparation, B.W.; writing—review and editing, Y.F.

Funding: This work was partly supported by the National Natural Science Foundation of China (11747114), Doctor Foundation of Jiangsu Normal University (16XLR022).

Conflicts of Interest: The authors declare no conflict of interest.

References

1. Nayak, A.K.; Nicklas, M.; Chadov, S.; Khuntia, P.; Shekhar, C.; Kalache, A.; Baenitz, M.; Skourski, Y.; Guduru, V.K.; Puri, A.; et al. Design of compensated ferrimagnetic Heusler alloys for giant tunable exchange bias. *Nat. Mater.* **2015**, *14*, 679–684. [[CrossRef](#)] [[PubMed](#)]
2. Graf, T.; Felser, C.; Parkin, S.S.P. Simple rules for the understanding of Heusler compounds. *Prog. Solid State Chem.* **2011**, *39*, 1–50. [[CrossRef](#)]
3. Galanakis, I.; Dederichs, P.H.; Papanikolaou, N. Slater-Pauling behavior and origin of the half-metallicity of the full-Heusler alloys. *Phys. Rev. B* **2002**, *66*, 174429. [[CrossRef](#)]
4. Skaftouros, S.; Özdoğan, K.; Şaşıoğlu, E.; Galanakis, I. Generalized Slater-Pauling rule for the inverse Heusler compounds. *Phys. Rev. B* **2013**, *87*, 024420. [[CrossRef](#)]
5. Feng, Y.; Chen, H.; Yuan, H.; Zhou, Y.; Chen, X. The effect of disorder on electronic and magnetic properties of quaternary Heusler alloy CoFeMnSi with LiMgPbSb-type structure. *J. Magn. Magn. Mater.* **2015**, *378*, 7–15. [[CrossRef](#)]
6. Özdoğan, K.; Şaşıoğlu, E.; Galanakis, I. Slater-Pauling behavior in LiMgPdSn-type multifunctional quaternary Heusler materials: Half-metallicity, spin-gapless and magnetic semiconductors. *J. Appl. Phys.* **2013**, *113*, 193903. [[CrossRef](#)]
7. Jourdan, M.; Minár, J.; Braum, J.; Kronenberg, A.; Chadov, S.; Balke, B.; Gloskovskii, A.; Kolbe, M.; Elmers, H.J.; Schönhense, G.; et al. Direct observation of half-metallicity in the Heusler compound Co₂MnSi. *Nat. Commun.* **2014**, *5*, 3974. [[CrossRef](#)] [[PubMed](#)]
8. Feng, Y.; Xu, X.; Cao, W.; Zhou, T. Investigation of cobalt and silicon co-doping in quaternary Heusler alloy NiFeMnSn. *Comput. Mater. Sci.* **2018**, *147*, 251–257. [[CrossRef](#)]
9. Wang, L.; Jin, Y. A spin-gapless semiconductor of inverse Heusler Ti₂CrSi alloy: First-principles prediction. *J. Magn. Magn. Mater.* **2015**, *385*, 55–59. [[CrossRef](#)]
10. Han, J.; Gao, G. Large tunnel magnetoresistance and temperature-driven spin filtering effect based on the compensated ferrimagnetic spin gapless semiconductor Ti₂MnAl. *Appl. Phys. Lett.* **2018**, *113*, 102402. [[CrossRef](#)]
11. Gao, G.Y.; Hu, L.; Yao, K.L.; Luo, B.; Liu, N. Large half-metallic gaps in the quaternary Heusler alloys CoFeCrZ (Z = Al, Si, Ga, Ge): A first-principles study. *J. Alloy. Compd.* **2013**, *551*, 539–543. [[CrossRef](#)]
12. Felser, C.; Wollmann, L.; Chadov, S.; Fecher, G.H.; Parkin, S.S.P. Basics and prospective of magnetic Heusler compounds. *APL Mater.* **2015**, *3*, 041518. [[CrossRef](#)]
13. Feng, Y.; Chen, X.; Zhou, T.; Yuan, H.; Chen, H. Structural stability, half-metallicity and magnetism of the CoFeMnSi/GaAs(0 0 1) interface. *Appl. Surf. Sci.* **2015**, *346*, 1–10. [[CrossRef](#)]
14. Knut, R.; Svedlindh, P.; Mryasov, O.; Gunnarsson, K.; Warnicke, P.; Arena, D.A.; Bjorck, M.; Dennison, A.J.C.; Sahoo, A.; Mukherjee, S.; et al. Interface characterization of Co₂MnGe/Rh₂CuSn Heusler multilayers. *Phys. Rev. B* **2013**, *88*, 134407. [[CrossRef](#)]
15. Rani, D.; Suresh, E.K.G.; Yadav, A.K.; Jha, S.N.; Varma, D.M.R.; Alam, A. Structural, electronic, magnetic, and transport properties of the equiatomic quaternary Heusler alloy CoRhMnGe: Theory and experiment. *Phys. Rev. B* **2017**, *96*, 184404. [[CrossRef](#)]
16. Yang, F.J.; Wei, C.; Chen, X.Q. Half-metallicity and anisotropic magnetoresistance of epitaxial Co₂FeSi Heusler films. *Appl. Phys. Lett.* **2013**, *102*, 172403. [[CrossRef](#)]
17. Scheike, T.; Sukegawa, H.; Furubayashi, T.; Wen, Z.; Inomata, K.; Ohkubo, T.; Hono, K.; Mitani, S. Lattice-matched magnetic tunnel junctions using a Heusler alloy Co₂FeAl and a cationdisorder spinel Mg-Al-O barrier. *Appl. Phys. Lett.* **2014**, *105*, 242407. [[CrossRef](#)]
18. Feng, Y.; Wu, B.; Yuan, H.; Chen, H. Structural, electronic and magnetic properties of Co₂MnSi/Ag(100) interface. *J. Alloy. Compd.* **2015**, *623*, 29–35. [[CrossRef](#)]
19. Fetzer, R.; Wüstenberg, J.P.; Taira, T.; Uemura, T.; Yamamoto, M.; Aeschlimann, M.; Cinchetti, M. Structural, chemical, and electronic properties of the Co₂MnSi(001)/MgO interface. *Phys. Rev. B* **2013**, *87*, 184418. [[CrossRef](#)]
20. Yamaguchi, T.; Moriya, R.; Oki, S.; Yamada, S.; Masubuchi, S.; Hamaya, K.; Machida, T. Spin injection into multilayer graphene from highly spin-polarized Co₂FeSi Heusler alloy. *Appl. Phys. Express* **2016**, *9*, 063006. [[CrossRef](#)]

21. Feng, Y.; Cui, Z.; Wei, M.; Wu, B. Spin-polarized quantum transport in Fe₄N based current-perpendicular-to-plane spin valve. *Appl. Surf. Sci.* **2019**, *466*, 78–83. [[CrossRef](#)]
22. Lkhagvasuren, E.; Ouardi, S.; Fecher, G.H.; Auffermann, G.; Kreiner, G.; Schnelle, W.; Felser, C. Optimized thermoelectric performance of the n-type half-Heusler material TiNiSn by substitution and addition of Mn. *AIP Adv.* **2017**, *7*, 045010. [[CrossRef](#)]
23. Casper, F.; Graf, T.; Chadov, S.; Balke, B.; Felser, C. Half-Heusler compounds: Novel materials for energy and spintronic applications. *Semicond. Sci. Technol.* **2012**, *27*, 063001. [[CrossRef](#)]
24. Chen, S.; Ren, Z. Recent progress of half-Heusler for moderate temperature thermoelectric applications. *Mater. Today* **2013**, *16*, 387–395. [[CrossRef](#)]
25. Bos, J.W.G.; Downie, R.A. Half-Heusler thermoelectrics: A complex class of materials. *J. Phys. Condens. Matter* **2014**, *26*, 433201. [[CrossRef](#)] [[PubMed](#)]
26. Wang, X.L. Proposal for a new class of materials: Spin gapless semiconductors. *Phys. Rev. Lett.* **2008**, *100*, 156404. [[CrossRef](#)] [[PubMed](#)]
27. Ouardi, S.; Fecher, G.H.; Felser, C.; Kübler, J. Realization of Spin Gapless Semiconductors: The Heusler Compound Mn₂CoAl. *Phys. Rev. Lett.* **2013**, *110*, 100401. [[CrossRef](#)] [[PubMed](#)]
28. Galanakis, I.; Özdoğan, K.; Şaolu, E.; Blügel, S. Conditions for spin-gapless semiconducting behavior in Mn₂CoAl inverse Heusler compound. *J. Appl. Phys.* **2014**, *115*, 093908. [[CrossRef](#)]
29. Jamer, M.E.; Assaf, B.A.; Devakul, T.; Heiman, D. Magnetic and transport properties of Mn₂CoAl oriented films. *Appl. Phys. Lett.* **2013**, *103*, 2–7. [[CrossRef](#)]
30. Feng, Y.; Bo, W.; Yuan, H.; Kuang, A.; Chen, H. Magnetism and half-metallicity in bulk and (100) surface of Heusler alloy Ti₂CoAl with Hg₂CuTi-type structure. *J. Alloy. Compd.* **2013**, *557*, 202–208. [[CrossRef](#)]
31. Bainsla, L.; Mallick, A.I.; Raja, M.M.; Coelho, A.A.; Nigam, A.K.; Johnson, D.D.; Alam, A.; Suresh, K.G. Origin of spin gapless semiconductor behavior in CoFeCrGa: Theory and Experiment. *Phys. Rev. B* **2015**, *92*, 045201. [[CrossRef](#)]
32. Galanakis, I.; Özdoğan, K.; Şaşıoğlu, E. Spin-filter and spin-gapless semiconductors: The case of Heusler compounds. *AIP Adv.* **2016**, *6*, 055606. [[CrossRef](#)]
33. Gao, G.Y.; Yao, K.L. Antiferromagnetic half-metals, gapless half-metals, and spin gapless semiconductors: The D0₃-type Heusler alloys. *Appl. Phys. Lett.* **2013**, *103*, 232409. [[CrossRef](#)]
34. Xu, G.Z.; Liu, E.K.; Du, Y.; Li, G.J.; Liu, G.D.; Wang, W.H.; Wu, G.H. A new spin gapless semiconductors family: Quaternary Heusler compounds. *EPL* **2013**, *102*, 17007. [[CrossRef](#)]
35. Bainsla, L.; Suresh, K.G. Equiatomic quaternary Heusler alloys: A material perspective for spintronic applications. *Appl. Phys. Rev.* **2016**, *3*, 031101. [[CrossRef](#)]
36. Perdew, J.P.; Burke, K.; Ernzerhof, M. Generalized gradient approximation made simple. *Phys. Rev. Lett.* **1996**, *77*, 3865. [[CrossRef](#)] [[PubMed](#)]
37. Blöchl, P.E. Projector augmented-wave method. *Phys. Rev. B* **1994**, *50*, 17953. [[CrossRef](#)]

